Ocean Engineering 338 (2025) 122039

Contents lists available at ScienceDirect

Ocean Engineering

journal homepage: www.elsevier.com/locate/oceaneng

Research paper

Numerical study of flow-sound correlation mechanism and sound source distribution for NACA0012 hydrofoil

Lianjie Yu [a], Decheng Wan [b,*], Qi Shen [a], Yan Gao [a], Jiaao Geng [a], Shang Shi [a]

[a] China Ship Scientific Research Center, Wuxi, China

[b] Computational Marine Hydrodynamic Lab (CMHL), School of Naval Architecture, Ocean and Civil Engineering, Shanghai Jiao Tong University, Shanghai, China

A B S T R A C T

Hydrofoil is a simplified model of the propeller. Its lifting surface is also widely used in the submarine sail, rudder and other structures. Focus on hydrofoil sound source distribution and flow-sound correlation mechanism, NACA0012 hydrofoil is selected as the research object. Large eddy simulation (LES) and acoustic analogy is used to study the flow and sound characteristics. Dual-mesh technology is applied for accelerating the computation. The numerical results are validated by experiments. It is found that the computational efficiency is improved by more than 30 times with no loss of accuracy using dual-mesh technique. Cross spectrum, third-generation vortex identification technique and DMD are used to analyze the mechanism of wall pressure fluctuation and vortex structure on the radiated noise. By calculating the cross-spectral correlation coefficients, it is found that the correlation is stronger at the *n*th order peak frequency. Both of dipole and wall pressure have extreme values in the suction and lifting direction. With dynamic mode decomposition (DMD), it is found that the vortices are similar to the dominant mode of the Lighthill source. The peak frequency of quadrupole corresponds to the high-energy mode of the vortex shedding.

1. Introduction

Hydrofoil is a typical underwater structure, which is highly valuable for engineering research (Zhang and Huang, 2023). As a simplified model of propellers, hydrofoils are suitable for studying the sound mechanisms. It has different boundary layers, separation vortices and other phenomena, which are of high scientific research value. The current research on hydrodynamic performance of hydrofoils are sufficient. However, its sound source distribution and the flow-sound correlation have not been investigated systematically, especially for the quadrupole sound pressure. Therefore, a more in-depth numerical study of hydrofoil flow noise is necessary.

The incoming flow develops from the leading edge, forms a turbulent boundary layer on the suction side. The velocity shear layer is developed in the outer layer (Ausoni et al., 2009). Due to the instability of the shear flow, disturbances appear in the trailing edge wake, which can generate additional noise (Daskovsky et al., 2000). Wu et al. (2013) conducted experiments on NACA0012 hydrofoil in different attack angles. They found that the separation point moves upstream with the increase of attack angles. And the phenomenon of separation bubbles occurs above the hydrofoil. Xu et al. (2017) conducted experiments and numerical simulations for the NACA66 (MOD) hydrofoil. They reveal that both the vibration noise and the flow noise reach the maximum near the vortex-shedding frequency.

LES is the recommended method to simulate hydrodynamic and acoustic problems. Zhi et al. (2022) observed a horseshoe vortex with LES. According to the vorticity transport equation, the vortex stretching and vortex dilatation effects are studied numerically. Deng et al. (2025) compared the performance of RANS, DES and LES for unsteay characteristics predictions. They found LES is suitable for detailed research. DES and RANS are better suited for large-scale flow and practical engineering application. Yu et al. (2022) studied the ventilated cavitating hydrofoil with LES and revealed the two fluctuation stages and mechanisms. Luo et al. (2022) compared POD (Proper Orthogonal Decomposition)and DMD results in numerical simulation for NACA0015 hydrofoil with LES method. The first four modes possessed 99.5 % energy in POD results, while DMD reveals the bridge role for the 2nd mode between the 1st mode and the 2nd mode. In conclusion, LES and DMD are suitable for detailed research in the turbulent flow.

Processing methods of acoustic formulas are introduced here briefly. The sound preditction is realized by acoustic analogy in most engineering problems. FW-H formulation is the common form in acoustic analogy. The FW-H equation is a partial differential fluctuation equation. A common treatment is to use Green's function integrals. There are many expressions for the integral solution, such as the Farassat 1A equation and so on (Yu et al., 2022). Most of them neglect the quadrupole source term. However, the research in recent years has shown that the effect of the quadrupole term cannot be ignored in some cases (Posa

* Corresponding author.
E-mail address: dcwan@sjtu.edu.cn (D. Wan).

https://doi.org/10.1016/j.oceaneng.2025.122039
Received 22 January 2025; Received in revised form 22 June 2025; Accepted 25 June 2025

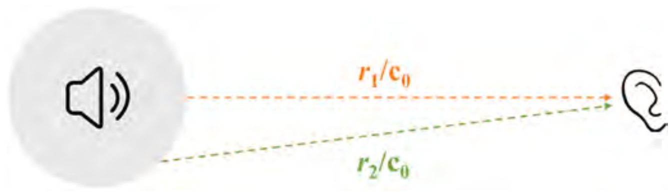

Fig. 1. The diagram of time delay effect for the same receiver.

et al., 2022). Although methods such as the permeable FW-H equation (Lockard and Casper, 2005) have appeared. However, this method is sensitive to the choice of the integrating surface and suffers from the 'End-cap' problem (Cianferra et al., 2018). Currently, the most accurate method for quadrupole computation is the direct volume integration. The direct volume integration not only accounts for the vortices-induced sources, but also overcomes the 'End-cap' problem as long as it wraps around the full vortices (Zhao et al., 2022). The disadvantage is its huge storage requirement and long computation time. In brief, FW-H formulation with volume integration for quadrupole is recommended.

There are two ways to overcome this shortcoming. One is data dimensionality reduction, based on decomposition algorithms and other means, to reduce the amount of flow field data (Gadalla et al., 2021). The other is to use dual-mesh technology, that is, the acoustic mesh and the CFD mesh are independent, and the sound source computation is carried out by interpolating from the CFD grid into the acoustic grid, thus reducing the computation amount (Wang et al., 2022). In conclusion, decomposition algorithms and dual-mesh technique are two ways to shorten the computation time when the volume integration is adopted.

The problem objects in this paper are all rigid. It is organized as follows: Firstly, the mathematical foundation is introduced, including large eddy simulation (LES), dual-mesh technique and dynamic mode decomposition (DMD). The acoustic method is validated by the underwater cylinder experiment at last. Secondly, the numerical setup and validation for NACA0012 hydrofoil is carried out. Thirdly, the sound source distribution is studied, including quadrupole and dipole source. Fourthly, the flow-sound correlation mechanism is investigated, focusing on pressure fluctuation and vortex shedding. Finally, the conclusion is given.

2. Mathematical foundation

2.1. Fluid dynamic field

The computational fluid dynamic (CFD) method is large eddy simulation (LES). It solves the filtered velocity and pressure in Navier-Stokes (N-S) equation. The filtered N-S equation is like

$$\frac{\partial \widetilde{u_i}}{\partial t}+\frac{\partial\left(\widetilde{u_i u_j}\right)}{\partial x_j}=-\frac{1}{\rho}\frac{\partial \widetilde{p}}{\partial x_i}+\nu\widetilde{\nabla^2 u_i} \tag{1}$$

where the superscript $\sim$ means the quantities after space filer. If the filer process is uniform filering, there is

$$\frac{\widetilde{\partial u_i}}{\partial t}=\frac{\partial \widetilde{u_i}}{\partial t} \tag{2}$$

$$\frac{\widetilde{\partial p}}{\partial x_i}=\frac{\partial \widetilde{p}}{\partial x_i} \tag{3}$$

$$\widetilde{\nabla^2 u_i}=\nabla^2\widetilde{u_i} \tag{4}$$

$$\frac{\widetilde{\partial\left(u_i u_j\right)}}{\partial x_j}=\frac{\partial\left(\widetilde{u_i u_j}\right)}{\partial x_j} \tag{5}$$

Therefore, N-S equation is transformed to

$$\frac{\partial \widetilde{u_i}}{\partial t}+\frac{\partial\left(\widetilde{u_i u_j}\right)}{\partial x_j}=-\frac{1}{\rho}\frac{\partial \widetilde{p}}{\partial x_i}+\nu\nabla^2\widetilde{u_i} \tag{6}$$

The convective term $\widetilde{u_i u_j}$ can be separated into $\widetilde{u_i}\widetilde{u_j}$ and $\widetilde{u_i u_j}-\widetilde{u_i}\widetilde{u_j}$. The former stands for the transport of momentum after filering, and the latter is the transport between sub-grid-scale (SGS) velocity and grid-scale velocity. For convenience, let $\tau^{SGS}=\widetilde{u_i u_j}-\widetilde{u_i}\widetilde{u_j}$. The filtered N-S equation is

$$\frac{\partial \widetilde{u_i}}{\partial t}+\frac{\partial\left(\widetilde{u_i}\widetilde{u_j}\right)}{\partial x_j}=-\frac{1}{\rho}\frac{\partial \widetilde{p}}{\partial x_i}+\nu\nabla^2\widetilde{u_i}+\nabla\cdot\tau^{SGS} \tag{7}$$

The term τ^{SGS} is named as SGS tensor stress. For the closed-form formulation, τ^{SGS} needs to be modeled. Accoding to the eddy visocity hypothesis (Smagorinsky et al., 1963), there is

$$\tau^{SGS}=\frac{2}{3}\mathrm{tr}\left(\nu^{SGS}\right)\mathrm{I}-2\nu_{SGS}\widetilde{S} \tag{8}$$

Here, tr( ) stands for diagonal entries of matrix. I is normal diagonal matrix. ν^{SGS} is the SGS viscocity coefficient. $\widetilde{S}=\frac{1}{2}\left(\frac{\partial\widetilde{u_i}}{\partial x_i}+\frac{\partial\widetilde{u_j}}{\partial x_j}\right)$ is called velocity strain rate. There are many ways to model ν^{SGS}. In this paper, Wall-adapted local eddy (WALE) model (Nicoud et al., 1999) is adopted. Because it could adjust the attenuation coefficient according to the wall grid scale. WALE model is like

$$\nu_{SGS}=\left(\frac{C_w^2\Delta}{C_k}\right)^2\frac{\left(\widetilde{S}_{ij}\widetilde{S}_{ij}\right)^3}{\left(\left(\widetilde{S}_{ij}\widetilde{S}_{ij}\right)^{5/2}+\left(\widetilde{S}_{ij}\widetilde{S}_{ij}\right)^{5/4}\right)^2} \tag{9}$$

In the formulation, C_w and C_k are constant determined by experiments. The $C_w=0.60$ and $C_k=1.40$ according to the literature (Nicoud et al., 1999). Δ is the wall grid size.2.2 Acoustic prediction

The acoustic prediction is carried out by acoustic analogy. Based on Farassat 1A formulation (Farassat et al., 1998), the quadrupole sound is considered by volume integration. For the problem of flow around a body, the hydrodynamic noise is divided into dipole and quadrupole terms:

$$\begin{aligned}4\pi p_L{}'(x,t)=&\int_{f=0}\left[\frac{\dot{p}\cos\theta}{c_0 r(1-M_r)^2}+\frac{\widehat{r}_i\dot{M}_i p\cos\theta}{c_0 r(1-M_r)^3}\right]_{ret}dS\\&+\int_{f=0}\left[\frac{p(\cos\theta-M_i\eta_i)}{r^2(1-M_r)^2}+\frac{(M_r-M^2)p\cos\theta}{r^2(1-M_r)^3}\right]_{ret}dS\end{aligned} \tag{10}$$

$$\begin{aligned}4\pi p_Q{}'(x,t)=&\frac{1}{c_0^2}\frac{\partial^2}{\partial t^2}\int_{f>0}\left\{T_{ij}\left[\frac{\widehat{r}_i\widehat{r}_j}{r^*}\right]\right\}_\tau dV+\frac{1}{c_0}\frac{\partial}{\partial t}\int_{f>0}\left\{T_{ij}\left[\frac{2\widehat{r}_r\widehat{r}_j^*}{r^*}+\frac{\widehat{r}_i^*\widehat{r}_j^*-R_{ij}^*}{\beta^2 r^{*2}}\right]\right\}_\tau dV\\&+\int_{f>0}\left\{T_{ij}\left[\frac{3\widehat{r}_i^*\widehat{r}_j^*-R_{ij}^*}{r^{*3}}\right]\right\}dV\end{aligned} \tag{11}$$

Here, $p_L{}'$ is dipole sound pressure and $p_Q{}'$ is quadrupole sound pressure. $(x,t)(y,\tau)$ are space-time coordinate for receiver and source respectively. $c_0=1400m/s$ means the sound velocity. $r=|x-y|$ is the vector from receiver to source and $\widehat{r}_i$ is normalized. $M_r=\frac{rv_i}{c_0}$ is Mach number and $1-M_r$ is called Dopler factor. $\cos\theta=n_i\cdot\widehat{r}_i$ means the angle between observer and normal direction of grid. $T_{ij}=\rho u_i u_j$ is Lighthill tensor stress. Other parameters in $p_Q{}'$ can be found in the literature (Cianferra et al., 2018).

It should be noted that the volume integration needs to consider the time delay effect. The time delay effect is the duration difference among the source region grids to the same receiver, as is shown in Fig. 1. If the source region (V) size is very small, it can be ignored. However, for high sound velocity (like underwater environment), this effect needs to be considered. In numerical computation, the geometric center of V ($\overline{y}$) should be found first. The duration of geometric center to receiver ($\Delta\overline{t}=$

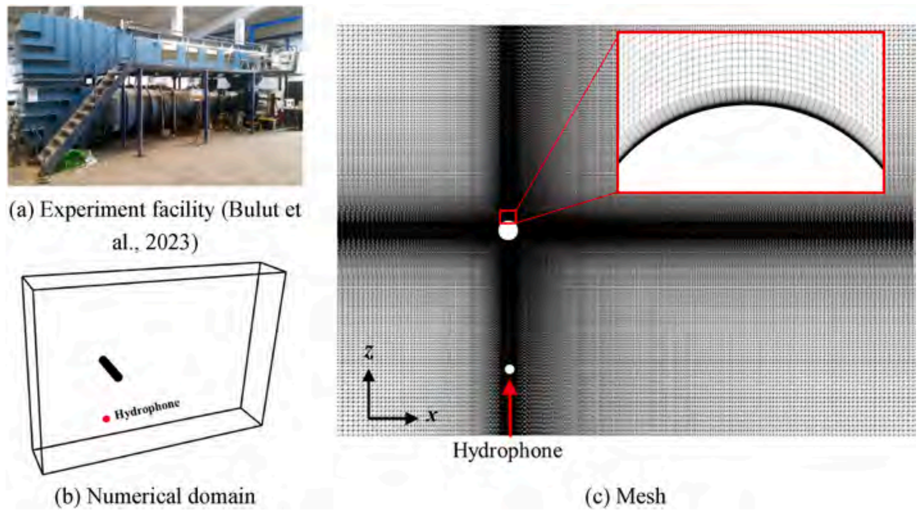

Fig. 2. The experiment setup, numerical domain and mesh for underwater cylinder.

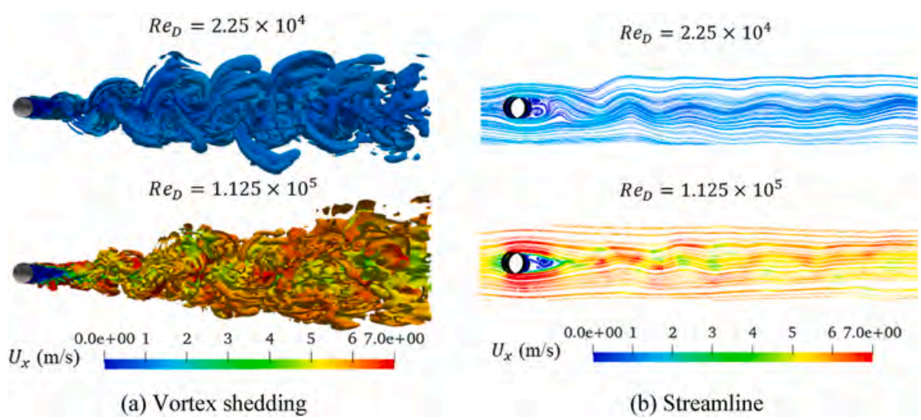

Fig. 3. The contour figure of Q = 100 s^{-2} and streamline for different working conditions: $Q = \frac{1}{2}\left(\|\boldsymbol{B}\|_F^2 - \|\boldsymbol{A}\|_F^2\right)$, where A and B is symmetric and antisymmetric tensors of velocity gradient.

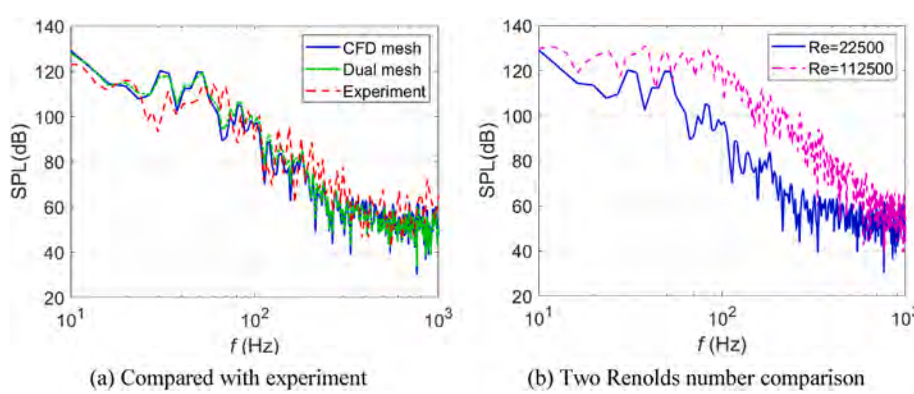

Fig. 4. The dual-mesh technique results compared with experiment and different Renolds number.

$\frac{|x-\bar{y}|}{c_0}$) is computed and stored. The duration for each source grid ($\Delta t' = \frac{|y-\bar{y}|}{c_0}$) is computed and substracted by $\Delta\bar{t}$. At last, the sound pressure is obtained by sum of all source grid at the same reaching time.

It is expensive to store all source grid time delay and impossible to integrate all source grids. To solve this problem, the dual-mesh technology is adopted and the codes is from (Wang et al., 2022). A coaser acoustic mesh is overlapped on the finer CFD mesh. The CFD mesh result (φ^{CFD}) is mapped on acoustic mesh ($\phi^{acoustic}$) by weighted summation. The weight is determined by the volume of grids (V^{CFD}):

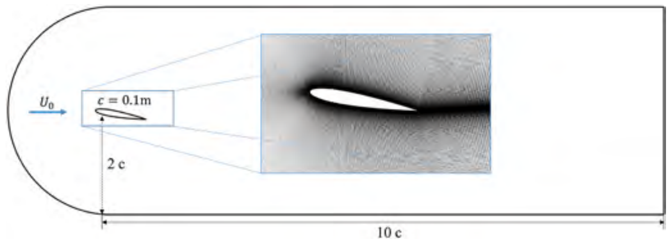

Fig. 5. Schematic diagram of computational domain and the mesh nearby.

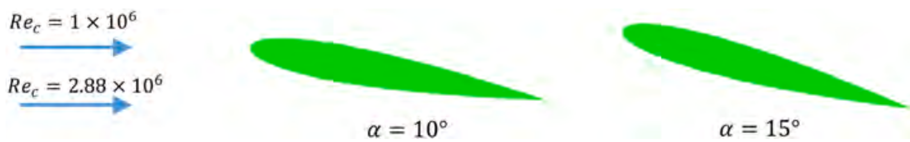

Fig. 6. Schematic diagram of angle of attack and inlet velocity for NACA0012 hydrofoil.

Table 1
The working conditions for flow around NACA0012 hydrofoil.

Case number	Renolds number (Re_c)	Attak angle (α)
NO.1	1×10^6	$10°$
NO.2	1×10^6	$15°$
NO.3	2.88×10^6	$10°$
NO.4	2.88×10^6	$15°$

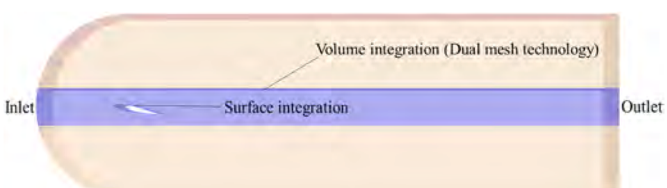

Fig. 7. The settings of integration range for NACA0012 hydrofoil radiated noise.

Table 2
The drag and lift force coefficients in $Re_c = 1 \times 10^6$ condition.

α	C_l (Exp)	C_l (LES)	C_d (Exp)	C_d (LES)	C_l (Error)	C_d (Error)
$10°$	1.0512	1.0189	0.0147	0.0142	3.07 %	3.40 %
$15°$	0.7108	0.7002	0.0245	0.0254	1.49 %	3.67 %

$$\phi_i^{acoustic} = \sum_{j=0}^{N_i} \varphi_{i,j}^{CFD} \cdot V_{i,j}^{CFD} \tag{12}$$

Here, φ and ϕ are any quantity on fluid field and acoustic field. The subscript i means the i^{th} acoustic element. The subscript (i,j) means the j^{th} fluid element of the i^{th} acoustic element.

The dual-mesh technique can improve the computation efficiency in two aspects. First, there are some derivative computation in the quadrupole sound prediction. Such derivative computation can be solved on coarser acoustic grids, which shortens the computation time. Second, because of time delay effect, the required stored grids are more. If the coarser acoustic mesh is adopted, the computation complexity is lessened. Although, this method reduces the revolution ratio of sound sources, the main features can be captured and the accuracy remains acceptable.

2.2. DMD method

Dynamic mode decomposition (DMD) has two applications. One is to realize data reduction, the other is to analyze the fluid field in different modes for mechanism study. This paper belongs to the latter. DMD is used to study the flow-sound correlation in this paper.

The foundation of DMD is linear transformation (Yin and Ong, 2020). Without loss of generality, a space-time sequence signal (U_{tx}) is defined. The subscript x is space position. The subscript t is time. Assuming there are N positions and m moments:

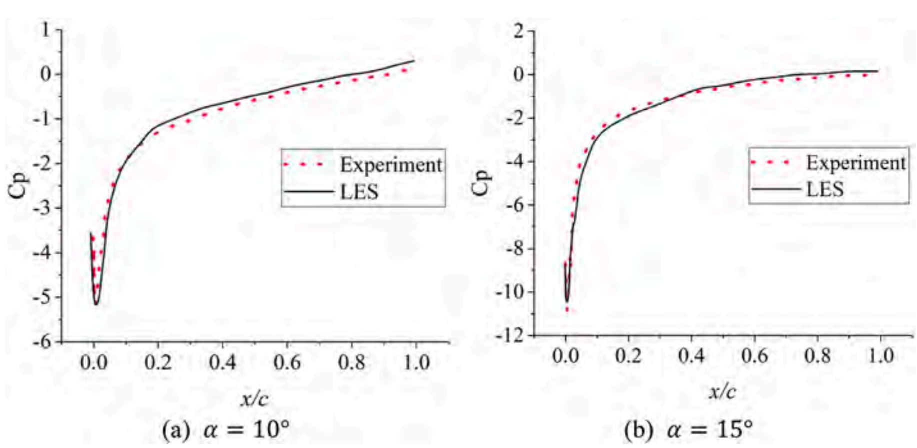

Fig. 8. The pressure coefficient on the suction side at $Re_c = 2.88 \times 10^6$ condition.

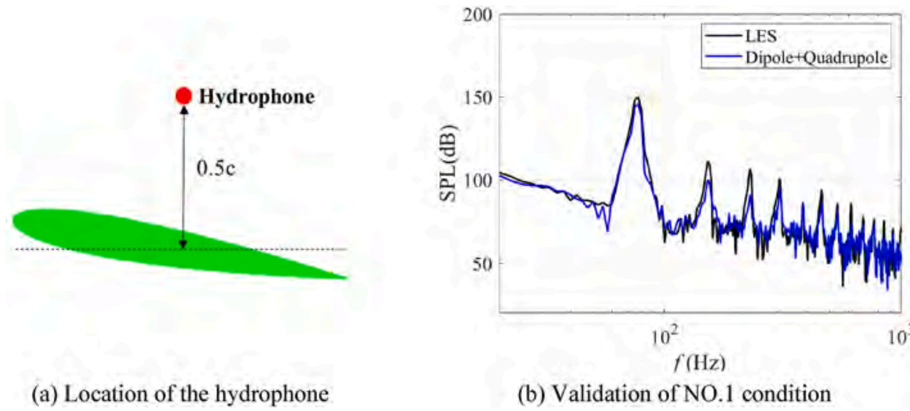

Fig. 9. The position of hydrophone and validation of NO.1 working condition.

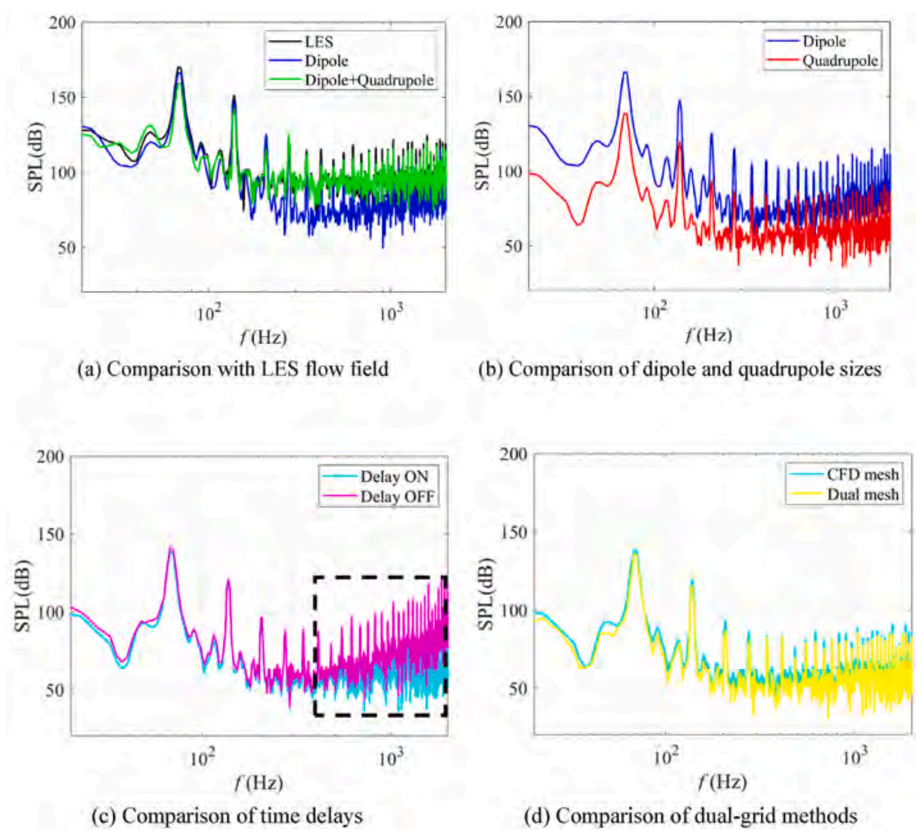

Fig. 10. The noise validation for different components and methods in NO.2 condition.

Table 3
Computation efficiency and accuracy of the dual-mesh technique for hydrofoil.

Mesh Type	Number of grids	Reference value/dB	Calculated value/dB	Error/dB	Calculation time/h	Efficiency gains
CFD mesh	4,113,000	–	141.4	–	842.5	–
Dual mesh	514,000	166.4	140.9	0.5	27.8	30.3 times

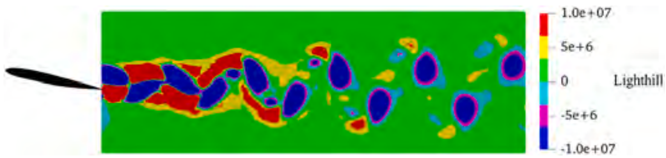

Fig. 11. The Lighthill source distribution in $\mathrm{Re_c} = 1 \times 10^6$ consdition for NACA0012 hydrofoil.

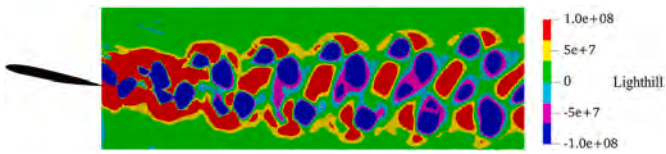

Fig. 12. The Lighthill source distribution in $\mathrm{Re_c} = 2.88 \times 10^6$ consdition for NACA0012 hydrofoil.

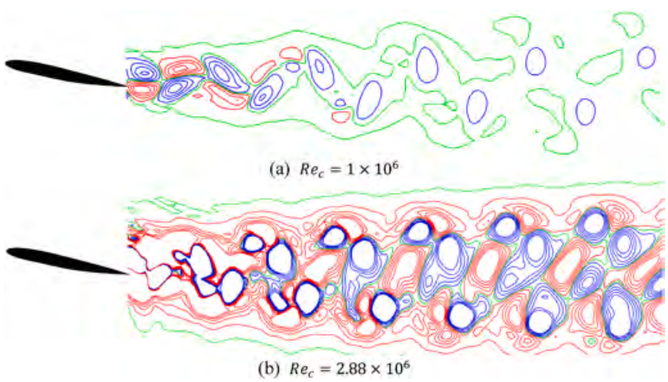

Fig. 13. The comparison for Lighthill source in different Renolds number at $\alpha = 10^\circ$ condition.

$$U_{tx} = \begin{bmatrix} u(t_1, x_1) & u(t_1, x_2) & \cdots & u(t_1, x_N) \\ u(t_2, x_1) & u(t_2, x_2) & \cdots & u(t_2, x_N) \\ \vdots & \vdots & \ddots & \vdots \\ u(t_N, x_1) & u(t_N, x_2) & \cdots & u(t_N, x_N) \end{bmatrix} \tag{13}$$

Extract the signal on the moment t_1 and transpose it. The signal U_{xt_1} is obtained:

$$U_{xt_1} = \begin{bmatrix} u(t_1, x_1) \\ u(1, x_2) \\ \vdots \\ u(t_1, x_1) \end{bmatrix} \tag{14}$$

In DMD, some linear transformation matrix (A) exists:

$$U_{xt_3} = A^* U_{xt_2} = A^{2*} U_{xt_1} \tag{15}$$

By theory, once the initial system U_{xt_1} is determined, the system U_{xt_k} at any moment (t_k) can be obtained by continued multiplication by transformation matrix (A). Further on, it can be written as:

$$U_{xt_k} = \sum_{i=1}^{m} b_i \cdot \lambda_i^k \cdot \phi_i \tag{16}$$

In this formulation, b_i is initial system. λ_i^k is the characteristics root of A. ϕ_i is the i^{th} mode. Besides, the characteristics root λ_i^k can be expressed in the damping form:

$$\lambda^k = e^{\mu \cdot kt} \tag{17}$$

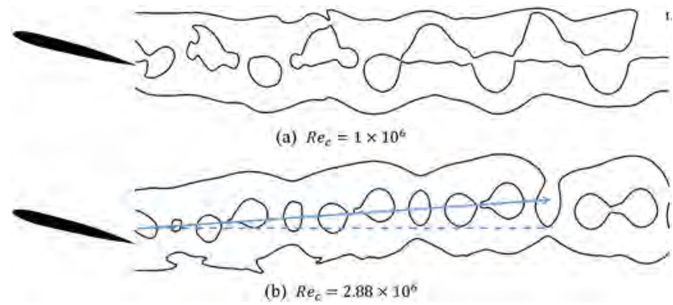

Fig. 14. The comparison for Lighthill source in different Renolds number at $\alpha = 15^\circ$ condition.

In summary, once the transformation matrix A is obtained, the characteristics roots (λ_i^k) and damping rate (μ) in each mode can be calculated (Kutz et al., 2016). Compared with other mode decomposition methods, for example, proper orthogonal decomposition (POD), DMD has an advantage: Each mode is corresponding to one frequency. This is beneficial to hydroacoustic analysis.

2.3. *Validation of acoustic method*

The validation of the dual-mesh technique is carried out with an underwater cylinder experiment, completed by Ata Nutku Laboratory in Istanbul Technical University (Bulut et al., 2023). The underwater noise experiments are shown in Fig. 2 (a). The hydrophone is located 5D down the cylinder, as shown in Fig. 2 (b). The numerical setting is the same as the experiment setup, with the cylinder diameter D = 0.019m and two Reynolds number conditions $\mathrm{Re_D} = 2.25 \times 10^4$ and $\mathrm{Re_D} = 1.125 \times 10^5$. The domain and mesh are as shown in Fig. 2 (c). The mesh within the boundary layer ensures that y^+ is less than 1, which meets the requirements of LES.

Comparing the flow at two Reynolds numbers, as shown in Fig. 3, some differences can be found. For example, the vortex distribution width of $\mathrm{Re_D} = 2.25 \times 10^4$ is not as wide as that of $\mathrm{Re_D} = 1.125 \times 10^5$ case. However, the vortex at high Reynolds number is more finely grained. This is due to the longer length of the return zone and the larger flow separation angle. These characteristics of the flow field will have an impact on the sound pressure.

The noise results compared with experiment in $\mathrm{Re_D} = 2.25 \times 10^4$ are shown in Fig. 4 (a). It can be seen that the errors between numerical prediction and experiment results are small, and the trend is consistent, indicating that LES can provide accurate inputs of sound sources, and the acoustic method is reliable. It is worth noting that the prediction results obtained by the dual-grid technique are almost the same as those by CFD mesh. Fig. 4 (b) shows the comparison between $\mathrm{Re_D} = 2.25 \times 10^4$ and $\mathrm{Re_D} = 1.125 \times 10^5$. Both the two working conditions use the dual-mesh technique to accelerate the volume integration, considering the time delay effect. It can be seen that the noise at high Reynolds is larger than that at low Reynolds number by about 10 dB. And their trends are slightly different. the high Reynolds number noise is higher than the low Reynolds number in the low-frequency range, while its decay in high frequencies is also more obvious.

3. Numerical setup and validation

In this chapter, the simulation results of NACA0012 hydrofoil at 2 attack angles and 2 Reynolds numbers will be compared with the experiments, including the coefficient of hydrofoil lift drag, pressure distribution, etc., to validate the accuracy of the large-vortex simulation methodology in hydrofoil bypassing problems. Due to the lack of experimental results for the acoustic field, and considering that the experimental comparison of non-cavitation noise has actually been done in the previous section, the results of the direct simulation of the LES will

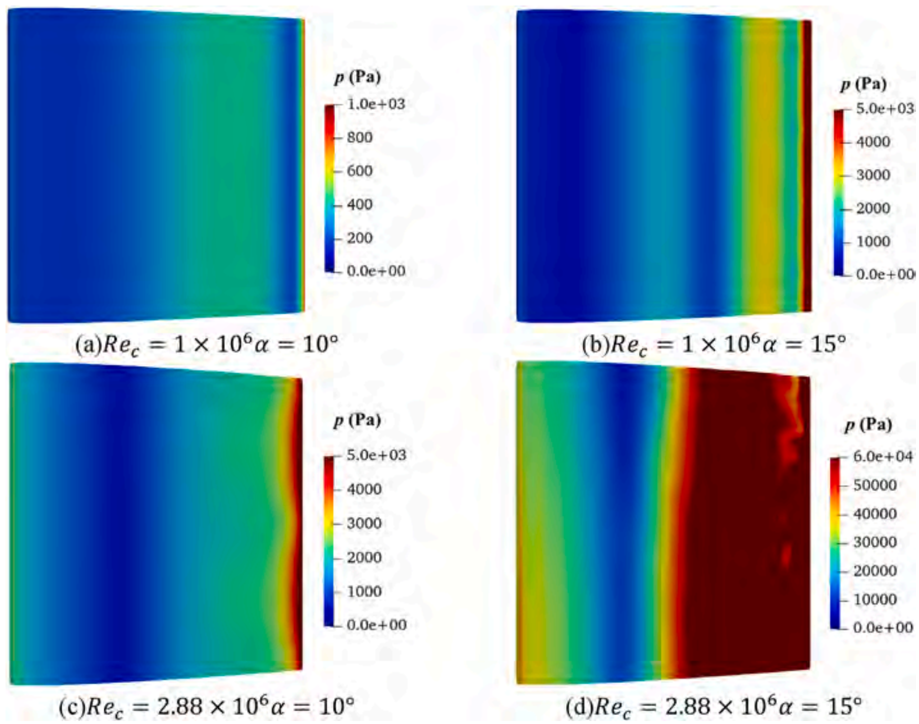

Fig. 15. The distribution of 'p' term in dipole on the suction side of NACA0012 hydrofoil.

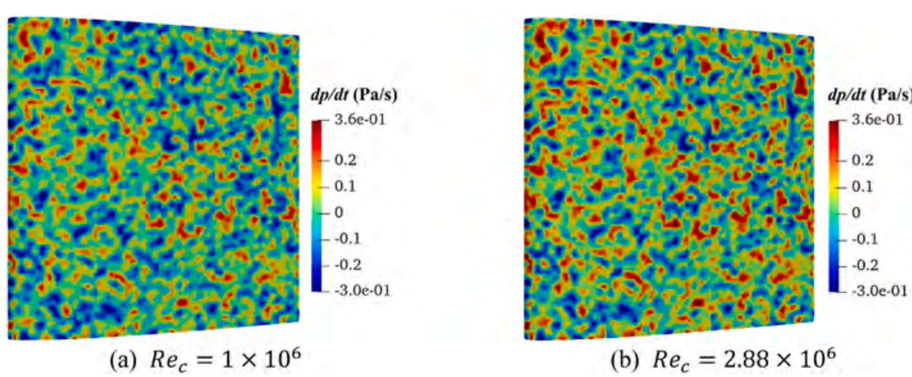

Fig. 16. The distribution of '*dpdt*' term in dipole on the suction side of NACA0012 hydrofoil.

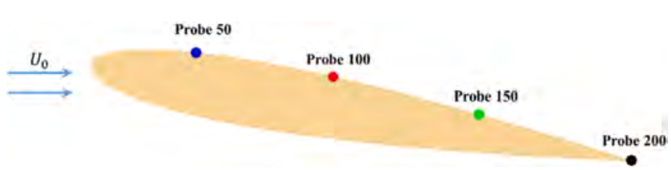

Fig. 17. Schematic diagram of typical wall pressure fluctuation locations on NACA0012 hydrofoil.

be used in this chapter as a reference to validate the results of the radiated noise prediction. This is in fact an acoustic validation method often used in the literature of numerical underwater noise prediction (Cianferra et al., 2018).

3.1. Case settings

The calculations are performed using NACA0012 standard hydrofoil with a chord length $c = 0.1\text{m}$. The spanwise length is $1c$. An infinite depth environment is adopted, with density $\rho = 1 \times 10^3 \text{kg/m}^3$ and ki-

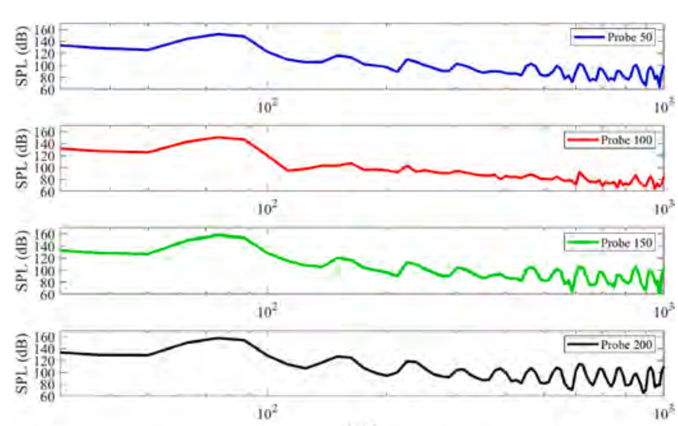

Fig. 18. The frequency spectrum of pressure fluctuation for $Re = 1 \times 10^6$, $\alpha = 10°$

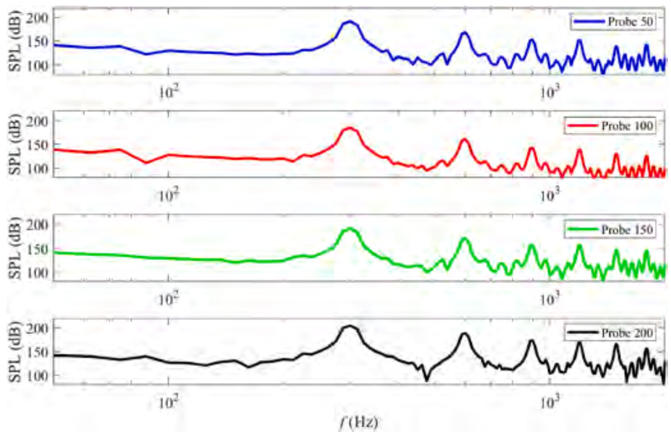

Fig. 19. The frequency spectrum of pressure fluctuation for $Re = 2.88\times 10^6$, $\alpha = 10^\circ$

nematic viscosity $\nu = 1\times 10^{-6}\mathrm{m}^2/\mathrm{s}$. The computational domain is shown as Fig. 5. The no-slip boundary type is used for both sides of the domain. The hydrofoil is far enough away from the inlet and outlet surface to avoid the reflection influence. A structured mesh with a total number of 21.7 million is adopted. The maximum value of x^+, y^+ and z^+ are 84, 0.89 and 22 respectively, meeting the requirements of the boundary layer. For the better capture of the vortex shedding behind the hydrofoil, the mesh is refined in the wake region, as shown in Fig. 5.

To investigate the flow and noise characteristics under different attack angles and different Reynolds numb Two attack angles, 10°and 15°, and two Reynolds numbers, 1×10^6 and 2.88×10^6 are selected to compare with the experiment results, as shown in Fig. 6. According to the combinations of attack angles and Reynolds numbers, there are 4 working conditions, namely NO.1-NO.4, as shown Table .1. The two angles are chosen to observe the differences in the flow field before and after the “stall” phenomenon, and how these differences affect the sound source and radiated noise. The time step is determined by the sound frequency range and Courant maximum number. To predict the sound within 2 kHz, the time step has to be smaller than 2.5×10^{-4} s considering the Shannon theorem. Under this premise, the time step should ensure the maximum Courant number less than 1. Combining the above, the time step for the case $\mathrm{Re_c} = 1\times 10^6$ is 1×10^{-5} s, while the step for $\mathrm{Re_c} = 2.88\times 10^6$ is 5×10^{-6} s. To avoid numerical oscillations, the linear upwind stabilized transport (LUST) scheme is adopted. LUST means a weighted average of 75 % linear central and 25 % linear upwind scheme. A second-order implicit backward difference method is employed in temporal terms, while the diffusion term is chosen as the Gaussian linear conservation scheme.

The noise is predicted based on the hydrofoil surface and the flow region around the hydrofoil (volume integration range), respectively, as is shown in Fig. 7. The integration on the hydrofoil surface represents the dipole sound pressure, and the volume integration represents the quadrupole sound pressure. The volume integration range is in a rectangle shape. It goes through the computational domain in the flow direction. Its height is 0.8 c. The volume intagration covers the whole span length. In this way, the range includes most of the quadrupole sources. The radiated noise calculations take into account the time delay effect. The accuracy and efficiency of the dual-mesh technique is analyzed for quadrupole sources.

A series of pressure fluctuation probes are set up to verify the pressure coefficient and are compared with the experiment. 200 probes are set on the hydrofoil suction surface at a spacing of 0.5 mm, used for the study of the wavenumber-frequency spectrum.

3.2. Validation of hydrofoil hydrodynamics

For the non-cavitating hydrofoil, the accuracy of the drag and lift

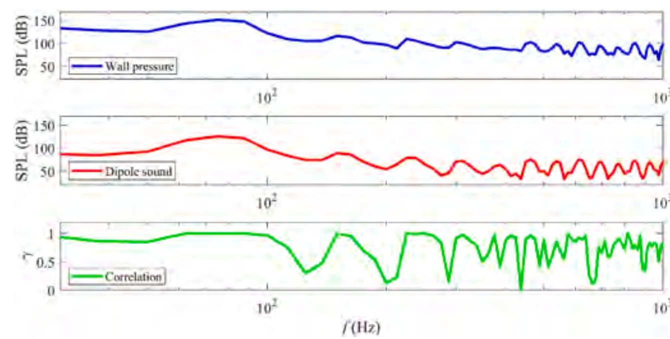

Fig. 21. The correltion between wall pressure and dipole sound for $Re = 1\times 10^6, \alpha = 10^\circ$

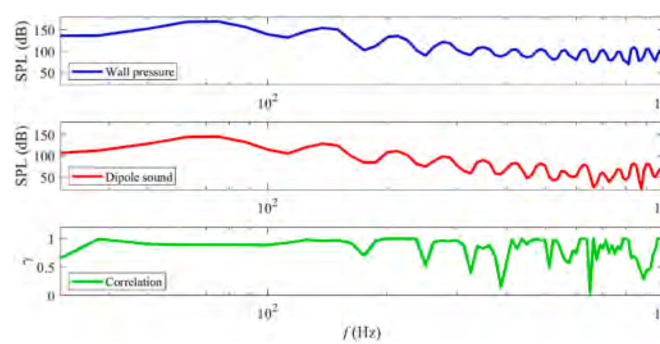

Fig. 22. The correltion between wall pressure and dipole sound for $Re = 1\times 10^6$, $\alpha = 15^\circ$

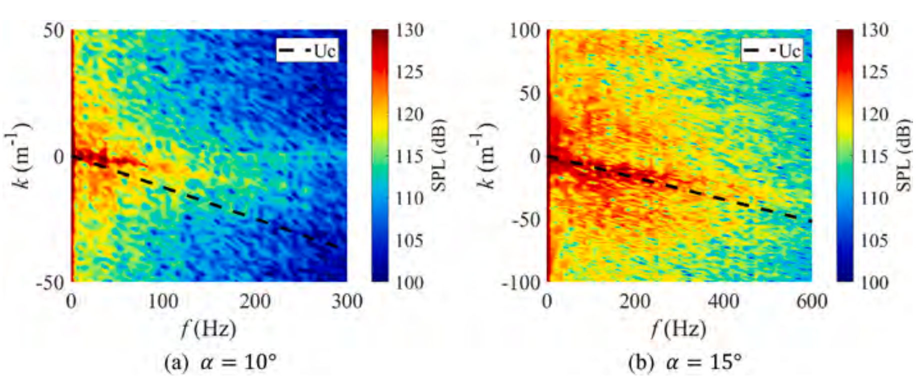

Fig. 20. The wavenumber-frequency spectrum for $Re = 1\times 10^6$ on NACA0012 hydrofoil.

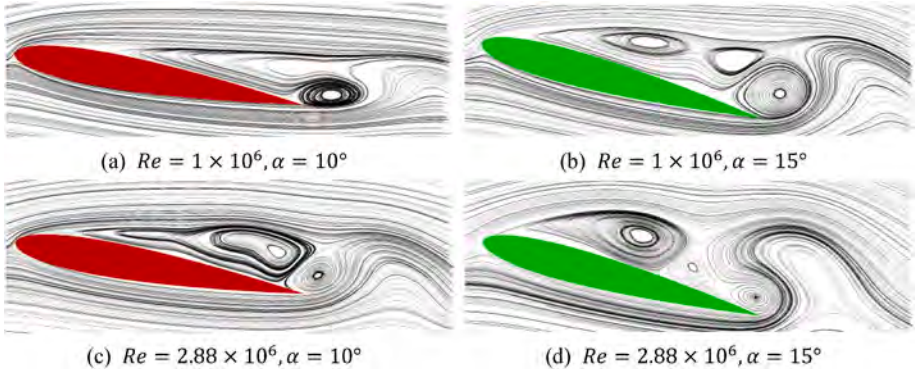

Fig. 23. The streamline near the hydrofoil suction side on one moment.

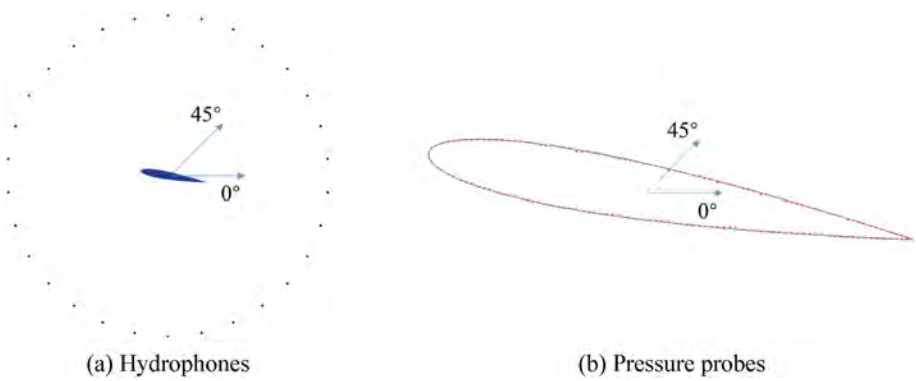

Fig. 24. The sketch view of hydrophones and wall pressure probes for direction research.

force is essential. After 400,000 iterations, the calculation results tend to be steady. At this time, the drag and lift time-history results are collected within 0.5s. Their average values are compared with the experiment results (Sheldahl et al., 1981). The dimensionless drag coefficient C_d and lift coefficient C_l are calculated as follows

$$C_d = \frac{F_d}{0.5\rho U_0^2 A} \tag{18}$$

$$C_l = \frac{F_l}{0.5\rho U_0^2 A} \tag{19}$$

F_d is the drag force on the hydrofoil; F_l is the lift force on the hydrofoil; ρ is the medium density, taken as $1 \times 10^3 \mathrm{kg/m^3}$; U_0 is the incoming flow velocity; A is the area of the hydrofoil.

As is shown in Table .2, the drag and lift force errors are less than 4 % compared with the experiments. It is worth noting that when the attack angle is 10°, the lift coefficient is much larger than that at 15°. Because at 15°, the "stalled" phenonmenon has accured, and the lift force decreases dramatically. In addition, it can be observed that the predicticted drag force is larger than the experimentresults, and the lift force is smaller than the experiment.

More microscopically, it is necessary to validate the pressure at different locations with experiments. The pressure coefficient C_p expression is defined as follows:

$$C_p = \frac{p - p_\infty}{0.5\rho U_0^2} \tag{20}$$

where p is the local local pressure on the hydrofoil surface; p_∞ is the pressure at the outlet surface, i.e. 0 Pa. The rest of the parameters have the same meanings as those in C_d and C_l.

The pressure data on the mid-span profile of the hydrofoil are extracted. Their time-averaged values are computed, and the pressure coefficient curve is ploted as shown in Fig. 8. The coordinates are made dimensionless by c for convenience. It can be seen that the pressure coefficient on the suction surface are negative, which directly leads to the upward lift of the hydrofoils. Overall, the pressure coefficients at both 10°and 15°are in good agreement with the experiment (Sheldahl et al., 1981). In fact, accurate prediction of pressure coefficients is very important for predicting radiated noise. Because one of the sound generation mechanisms is the pressure change on the hydrofoil surface.

The geometry, angle of attack, and velocity of the foil in the experiment are consistent with the simulated conditions, and the difference in Reynolds number is mainly due to the difference in density. This is not expected to have a significant impact on the prediction accuracy. In fact, many methods have been applied underwater after being proven effective in wind tunnels.

3.3. Validation of hydrofoil noise

Due to the lack of experiment data, the direct pressure result from LES in the near field is used as a reference to evaluate the error. The hydrophone is above the hydrofoil suction surface (center of the chord), at a height of 0.5c, as is shown in Fig. 9 (a). Fig. 9 (b) gives the comparison between the acoustic prediction and the reference data. It can be seen that the error is small. The sound pressure prediction is obtained by linear superposition of dipole and quadrupole sound pressure time calendar results, where the dipole sound pressure prediction uses the hydrofoil area fraction and the quadrupole sound pressure prediction uses the volume fraction of the range shown in. It can be seen that the predicted radiated noise captures the peak frequencies of all orders, though the magnitude is lower than the reference data slightly (see Fig. 10).

To verify each component of the radiated noise, the "dipole + quadrupole" results and "dipole" results obtained by surface integration are compared with the LES reference results (taking the NO.2 case as an example). As Fig.10 (a) shows, after adding the quadrupole component

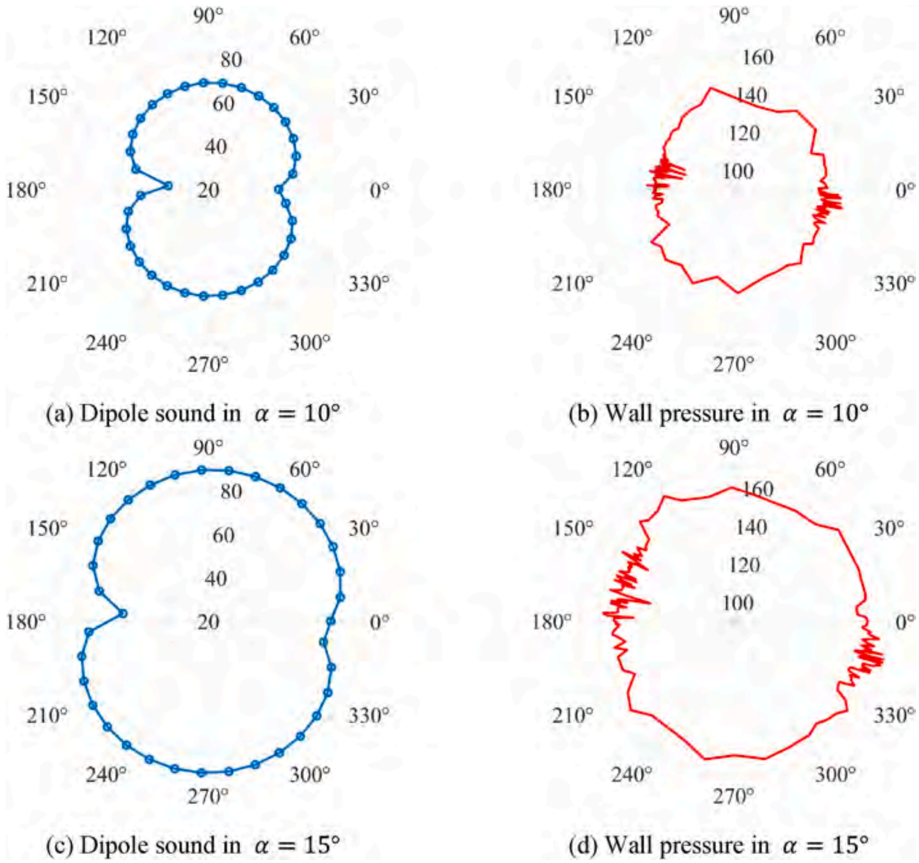

Fig. 25. The directivity of dipole noise and wall pressure fluctuation in $Re = 1 \times 10^6$ condition.

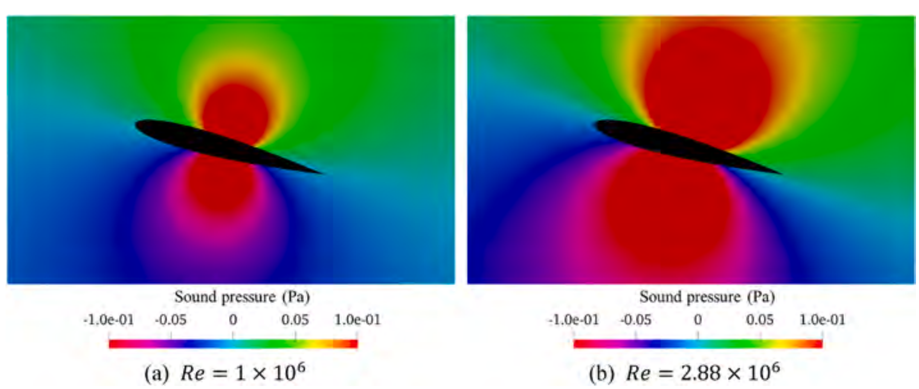

Fig. 26. The dipole sound pressure distribution at 15°attack angle.

obtained by volume integration, the noise prediction results are closer to the referece data, especially in the high-frequency bands. It implies that it is necessary to consider the quadrupole component for sound pressure prediction.

Fig.10 (b) shows a comparison of the dipole sound and quadrupole sound in NO.2 condition ($Re_c = 1 \times 10^6$; $\alpha = 15°$). It can be seen that they have the same peak frequencies. However, their magnitudes are different in some way. The difference is more obvious in the high frequency region. After about 300 Hz, the dipole sound pressure decays faster, while the quadrupole decays slowly. A large attack angle of 15°may contribute to the increased influence of the quadrupole, since a more powerful vortex is an important source of high-frequency noise.

Fig.10 (c) shows the effect of the time delay for quadrupole sound. It can be seen that the difference is in the high-frequency part, as is shown in the black boxed area. The sound pressure without time delay shows a high-frequency upward drift above 800 Hz, while the sound pressure with time delay do not show this phenomenon. Such high-frequency drift is unphysical due to numerical oscillations. It should be noted that this cutoff frequency does not strictly correspond to the MFP standard. However, this does not mean that MFP criterion is not applicable. In fact, the MFP value is close to 1 in this case, so that time delay effects still need to be taken into account.

Fig.10 (d) compares the quadrupole sound pressure with and without the dual-grid technique. It can be seen that the difference is small and the error is negligible. This proves that the dual-grid technology does not reduce the sound pressure accuracy significantly. The treatment makes the number of acoustic grids reduced to 1/8 of the CFD mesh, which greatly reduces the memory storage and improves the computation efficiency. Table .3 gives the quantitative performance of the dual-mesh technique. It can be seen that the error increases by only 0.5 dB, while

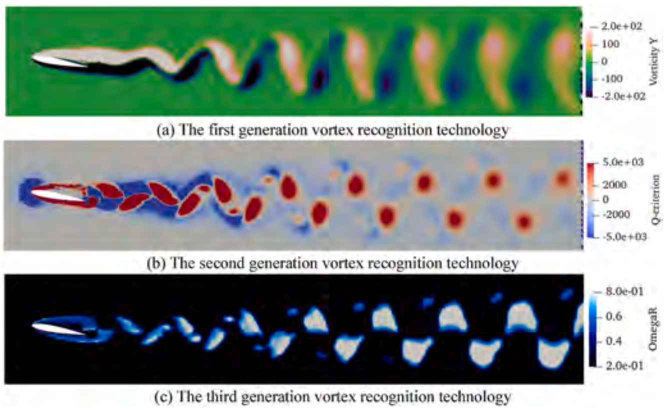

Fig. 27. The slice of vortex shedding with three methods.

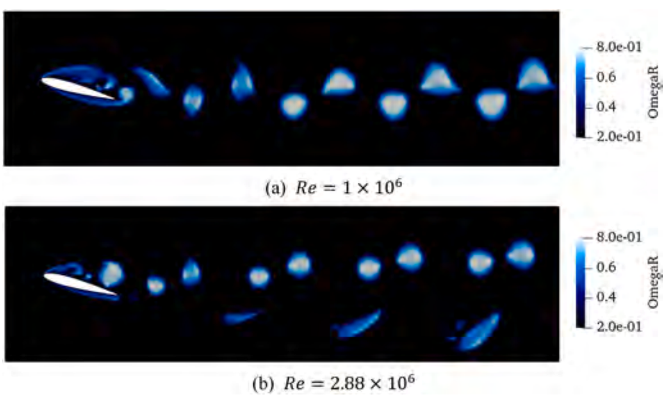

Fig. 28. The slice of vortex shedding with the third generation vortex technique.

the computation efficiency is improved by 30 times. Therefore, the subsequent prediction is computed by the dual-mesh technique to accelerate the prediction.

4. Sound source distribution

Non-cavitating hydrofoil sound sources can be divided into two types: quadrupole and dipole sources. The quadrupole sources are distributed throughout the flow field space, while the dipole sources are distributed on the object surface.

4.1. Quadrupole source distribution

The quadrupole cloud map is plotted in the range of 6c downstream, as shown in Fig. 11 and Fig. 12. Compared with the $\mathrm{Re}_c = 1\times 10^6$ case, the quadrupole intensity in the $\mathrm{Re}_c = 2.88 \times 10^6$ case is improved by one order of magnitude. The higher the Reynolds number, the wider the distribution range of the quadrupole sound source.

The quadrupole source contours are shown in Fig. 13. In this paper, such one-to-one coherent structure of quadrupole is named “Lighthill source pair”. It can be seen that there is only one Lighthill source pair for the $\mathrm{Re}_c = 1 \times 10^6$ case, while up to 2–4 pairs for the $\mathrm{Re}_c = 2.88\times 10^6$ case at the same steamwise section. It proves that the source density of the high Reynolds number is higher than that at low Reynolds number case.

The quadrupole contour at 7×10^6 value is plotted in Fig. 14. This value is chosen because it is equal to the threshold intensity of each Lighthill source pair. It provides a more distinct view of the source profile. It is found that the downstream sources is parallel along the flow at $Re_c = 1 \times 10^6$, while it shifts to the suction side at $Re_c = 2.88 \times 10^6$. The slope angle is measured to be 5°approximately. This shift is due to the flow separation occurring near the leading edge at high Renolds number. In low Reynolds numbers cases, the flow separation is dominated by the trailing separation, showing a clear downstream development trend.

4.2. Dipole source distribution

For the hydrofoil in this paper, there is no monopole source because of still station, nor is there a sphere source due to no cavitation. Only quadrupole and diple exist. The dipole sound source is distributed on the object surface.

Accoding to Farrassat 1A formulation, the dipole source can be divided into a ‘*p*’ term and a ‘*dpdt*’ term. The standard deviation (std) of the ‘*p*’ term is shown in Fig. 15. At 10° attack angle, the ‘*p*’ term is mainly concentrated at the trailing edge. For the larger attack angle, there is a wider region with larger sound source intensity. The effect of the Reynolds number is more obvious. At $e_c = 2.88 \times 10^6$, the ‘*p*’ term no longer shows a regular continuous band, but becomes more fragmented, and the region with large absolute value is increased. This is because it undergoes a drastic flow separation and does not experience a reattachment process on the suction surface.

Fig. 16 shows the distribution of the ‘*dpdt*’ term for the dipole sound source. It can be seen that this term is much smaller in magnitude compared to the ‘*p*’ term. Meanwhile, it shows a random distribution, which is similar to the fluctuating pressure in the plane turbulent boundary layer (Ching et al., 2006). This is because the suction surface is almost in turbulence entirely.

5. Pressure fluctuation correlation mechanism

The main source of dipole sound is the pressure fluctuation (‘*p*’ term). To understand the influence mechanism of the fluctuating pressure on the radiated noise, it is necessary to know the spectral and spatial distribution of the pressure fluctuation, finally to explain these distributions and correlations through the flow field.

5.1. Pressure fluctuation characteristics

To capture the fluctuating pressure characteristics, 200 measurement points are arranged on the suction surface in the hydrofoil span. The 50th, 100th, 150th, and 200th measurement points are selected as typical locations as shown in Fig. 17.The frequency spectrum is computed by the welch method, which ensures the energy conservation by employing a window function, and the overlap rate of the window function was set to 0.5 to minimize the variance. The sampling period is 4×10^{-5} s and the duration is 0.1s.

The frequency spectrum for $Re = 1 \times 10^6$ and $Re = 2.88 \times 10^6$ are plotted in Fig. 18 and Fig. 19 respectively. There is a clear narrow-band characteristic, with the peak frequency being about 90Hz at $Re = 1 \times 10^6$, while it being about 200Hz at $Re = 2.88 \times 10^6$. As the probe moves towards the trailing edge, the spectrum magnitude at the first-order peak increases gradually. Besides, the line-spectrum characteristic at 15°attack angle is more obvious than that at 10°.To prevent repetition, it is not shown here.

To study the spatial characteristics of the pressure fluctuation, the wavenumber-frequency spectrum is shown in Fig. 20. As can be seen from the figure, the larger the attack angle, the higher the energy. In terms of spatial and temporal correlation, “convective ridges (He et al., 2017) similar to those in the flat plane boundary layer can be observed. This is due to the fact that most of the hydrofoil suction surface is in the turbulent region, where the “Taylor freezing assumption” (Del Álamo and Jiménez, 2009) still holds. The convective velocity is different at the two attack angles. At 10°, the convective velocity is about 0.6 times the incoming velocity, while at 15°, it becomes 0.5 times the incoming

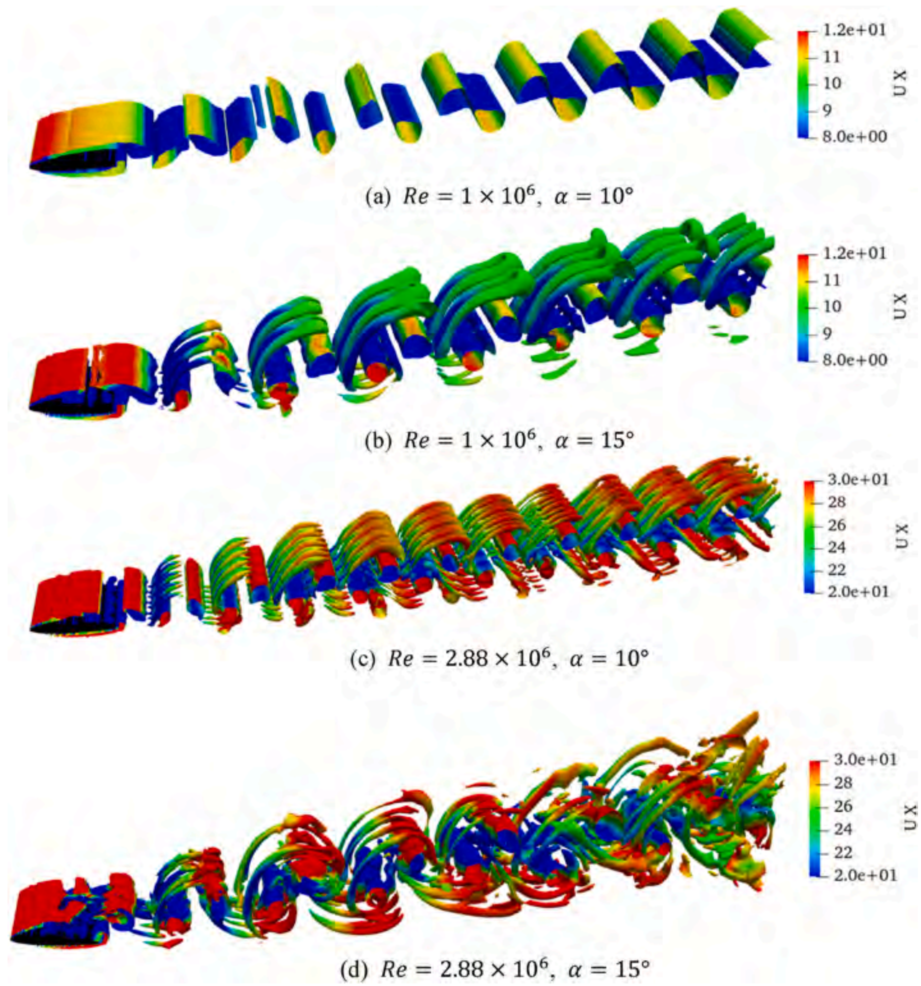

Fig. 29. The 3D vortex shedding contour for NACA0012 hydrofoil in different conditions.

velocity and the convection peaks seem “wider".

5.2. Correlation between pressure fluctuation and radiated noise

Dipoles noise is strongly associated with surface pressure. In this subsection, the frequency correlation between the fluctuating pressure and the dipole radiated noise is investigated by the cross spectrum. As is shown in Fig. 21, the measurement point is selected as ‘Probe 50’ and the hydrophone is 1c above the suction side. It can be seen that the correlation between fluctuating pressure and dipole radiated noise is stronger at the nth-order peak frequencies and weaker at other frequencies.

At 15°attack angle, the correlation coefficients are not only large at the peak frequencies, but also in a band near these frequencies, as is shown in Fig. 22. In addition, it is found that the pressure fluctuation becomes less correlated with the dipole noise under high Reynolds number conditions, which may be due to the fact that the flow is more turbulent and random.

To explain such frequency dependence, the streamlines are plotted in Fig. 23. It can be seen that at lower Reynolds numbers, there is no strong interference between the laminar separation bubbles developed on the leading edge and the following vortices developed on the trailing edge. The two are not mixed, which makes the fluctuation not influenced by the wake flow. However, at high Reynolds numbers, it is clear that the laminar separation bubble and the following edge vortex mix with each other. The interference of the wake may be the reason for the reduced correlation between the pressure fluctuation and the dipole radiated noise.

5.3. Effect of pressure fluctuation on acoustic directivity

To investigate the effect of pressure flucatuation on acoustic directivity, a round of hydrophones is set in the mid-section plane with a 20c distance as the radius. Thirty-six hydrophones are arranged in the circle uniformly, used to map the acoustic directivity. At the same time, a number of pressure probes are set on the hydrofoil surface for a round to investigate the correlation with acoustic directivity, as shown in Fig. 24. The scale of Fig. 24 has been zoomed somewhat for ease of presentation.

Fig. 25 gives a directivity plot of dipole sound pressure versus hydrofoil wall pressure. The overall sound pressure level or power spectral level is computed in the frequency range from 20 Hz to 2000 Hz. This is because most of the peak frequencies are in this range. It is considered to include most of the acoustic energy. From Fig. 25, it can be seen that the dipole sound and wall pressure show an obvious correlation feature in directionality. Both of them have great values in the direction of suction surface and lift surface. With the change of the attack angle, the direction of the maximum energy also changes. This indicates the existence of an important role of fluctuating pressure on the dipole sound directivity distribution.

However, there are some differences between the two. For example, the fluctuating pressure is actually smaller in the lifting side direction, while the dipole sound pressure shows extreme values in the suction side

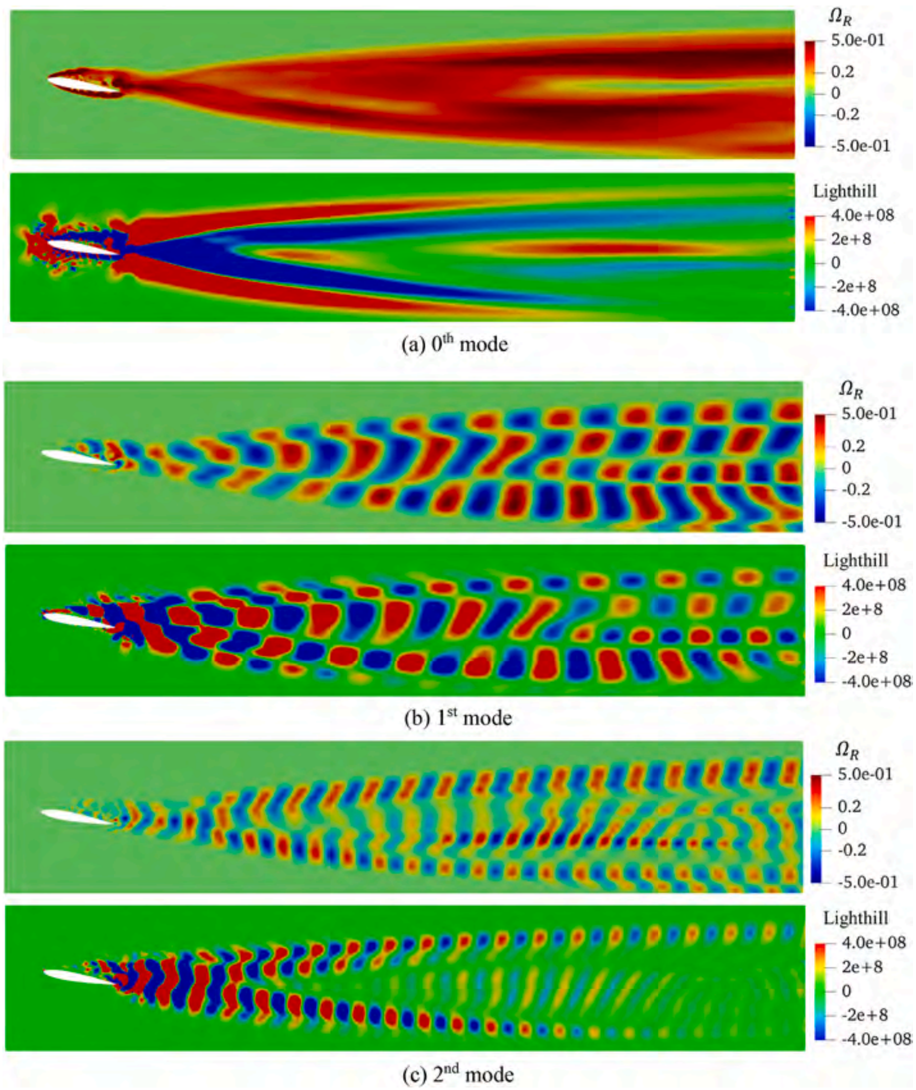

Fig. 30. The comparison of Lighthill source and vortex distributions in the first three modes.

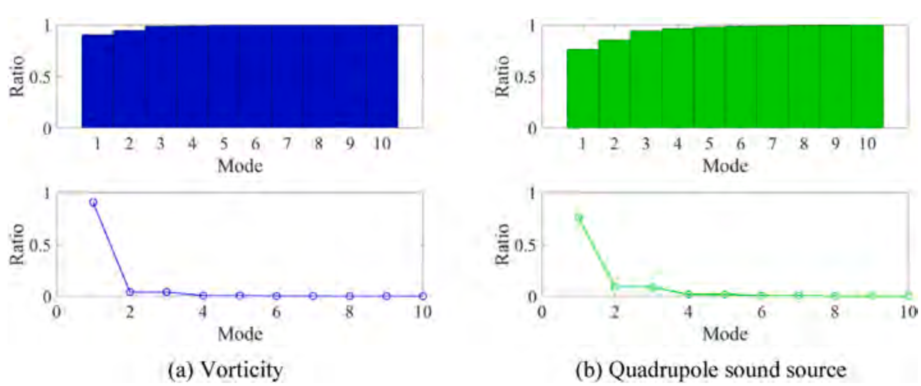

Fig. 31. The mode energy of Lighthill source and vortex at $\alpha = 10^{\circ}$

direction. The effect of the attack angle change on the wall pressure is comparable to that on the SPL, with both increasing by 10–20 dB from the 10°to 15°attack angle case. For the fluctuating pressure, the randomness seems to be greater in the lifting and suction sides, but both have extreme values near the hydrofoil tip.

The instantaneous cloud map of dipole sound pressure is plotted in Fig. 26. It can be seen that the high-energy region is almost perpendicular to the hydrofoil, showing a regular "8″ symmetric distribution in the suction and lifting side. Meanwhile, it can be seen that the dipole sound pressure at $Re = 2.88 \times 10^6$ is significantly higher than that at $Re = 1 \times 10^6$. Such distribution is similar to the pressure fluctuation directivity.

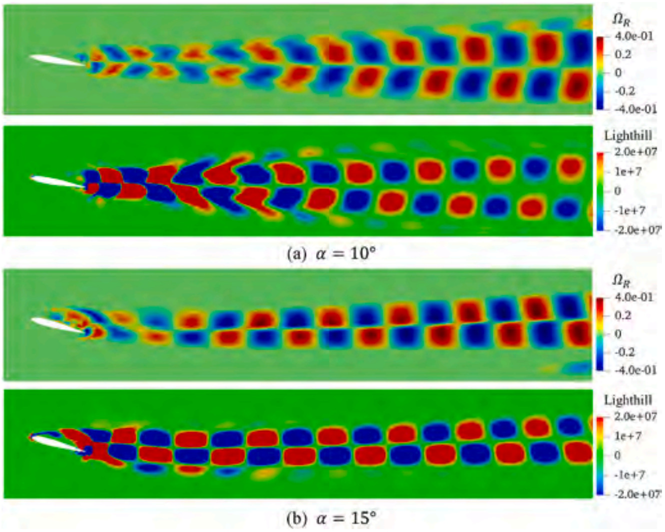

Fig. 32. Lighthill source and vortex distributions at different attack angles in 1st mode.

6. Vortex shedding correlation mechanism

The vortex shedding has an impact on hydrodynamic noise, especially quadrupole noise. The vortex structure of hydrofoils will be studied in this section. The advantages and disadvantages of different vortex identification techniques will be compared. DMD method will be used to perform modal decomposition on the vortex and Lighthill source. Their correlation in frequency and spatial distribution will be analyzed.

6.1. Characteristics of vortex structure in hydrofoil flow

Unless the flow on both sides is completely symmetrical and the trailing edge is sharp, hydrofoils generally experience some form of vortex shedding (Ghassemi et al., 2015). The vortex shedding behind the hydrofoil is similar to the Karman vortex street, and its peak frequency is positively correlated with the incoming velocity (Hu et al., 2020). The shape of the trailing edge also affects the strength of the wake vortex. The thicker the cross-section of the trailing edge, the stronger the vortex shedding, and the lower the peak frequency. The wake vortex at the trailing edge is crucial for the noise line-spectrum characteristics. The contribution of the trailing edge is generally greater than that of the leading edge. This is because there are different forms of vortex shedding in the wake.

For hydrofoils, vortex structures are concentrated in the wake region. Fig. 27 shows the cloud maps of vortices in the midspan section, which are drawn with three kinds of vortex identification techniques (Yu et al., 2022). It can be seen that the vortex detached from the hydrofoil and continued downstream at a distance of 10c. This implies the importance of quadrupole sound. Comparing the three vortex techniques, it can be found that both the Q criterion and vorticity ways display false vortices near the boundary. However, the third-generation vortex technique does not have such problems.

Fig. 28 shows the vortex distribution at two Reynolds number with the third generation vortex technique. It can be seen that the vortex recognition technology can capture the position of the vortex core accurately downstream of the hydrofoil. Whether it is the first generation vortex technology or the second generation one, it is difficult to uniquely determine the range of vortex cores. Because the values of Q and vorticity affect the distribution range of vortex cores greatly. However, there is no such issue for Ω_R as it is the result of strict normalization.

After verification, $\Omega_R = 0.52$ is the most effective value for capturing vortex cores, as shown in Fig. 29. The figure is colored by velocity. It can be seen that at low Reynolds numbers and low attack angles, the three-dimensional characteristics are not obvious. As the attack angle increases, the spanwise continuous vortex structure begins to break, forming structures similar to horseshoe. Fig.29 (b) demonstrates that at high Reynolds numbers, spanwise strupture occurs, enhancing the three-

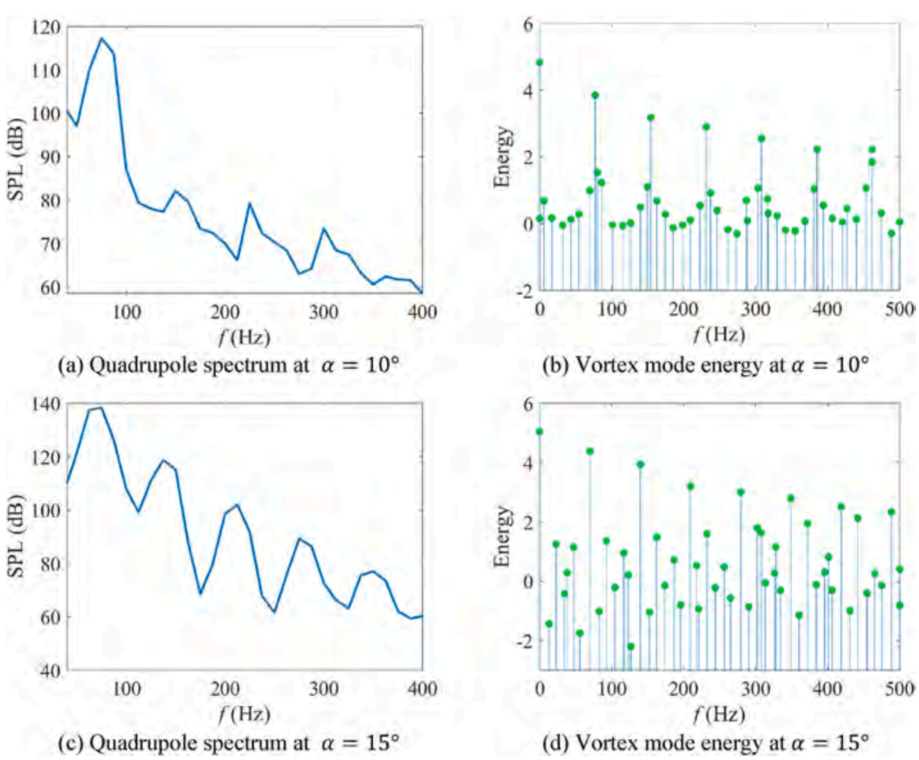

Fig. 33. The comparison of quadrupole noise and vortex modes in frequency for $Re = 2.88 \times 10^6$

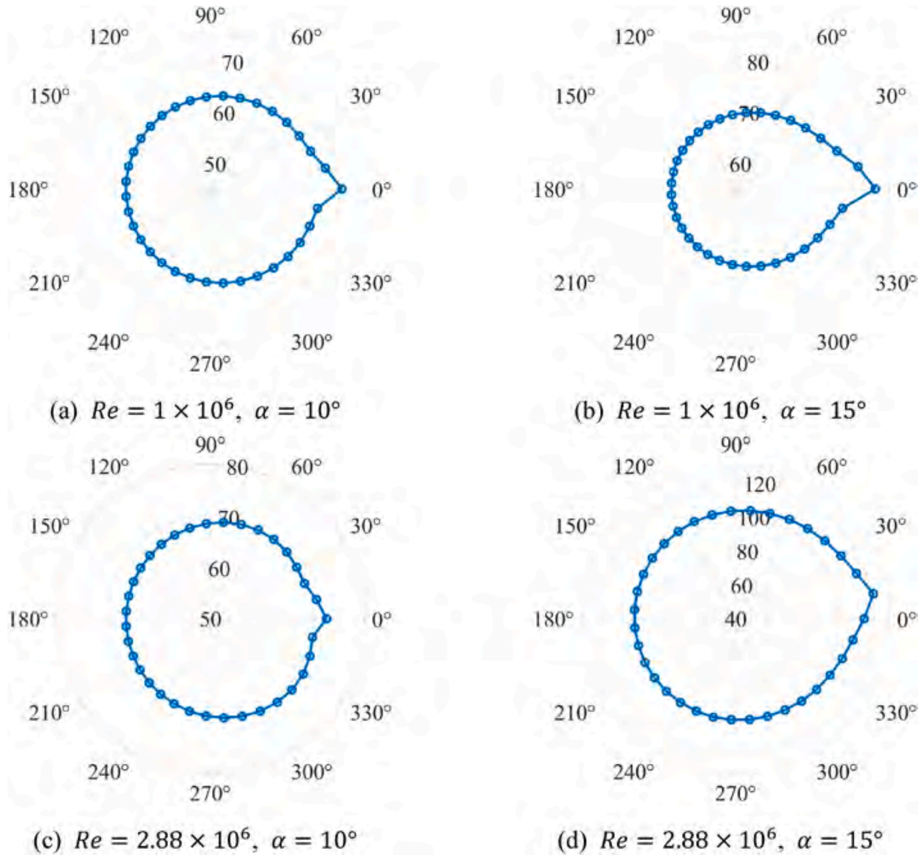

Fig. 34. The quadrupole sound directivity for NACA0012 hydrofoil in different conditions.

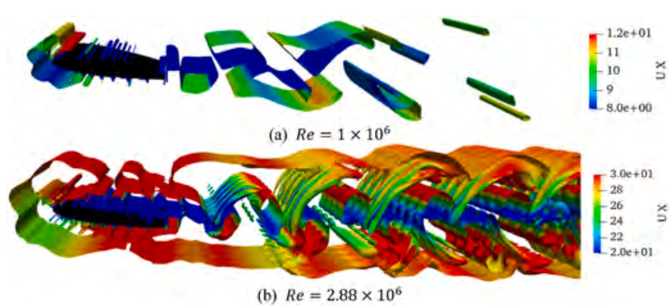

Fig. 35. The Lighthill source contour in $\alpha = 10°$ condition (Lighthill $= 1 \times 10^7$).

dimensional effect. Fig.29 (d) shows that at an attack angle of 15°, the instability is enhanced, and the coherence of the spanwise vortex disappears gradually. As the vortex moves downstream, random fragmentation and distortion begin to occur. Overall, for low Reynolds numbers and small attack angles, the vortices exhibit a clear paired distribution. The distance between vortex pairs at 15° attack angle is greater than that at 10°. This is correlated to the vortex shedding frequency, which is 10–20 Hz greater at 15 °than at 10° attack angle.

6.2. Correlation between vorticity and quadrupole sound source

In order to study the correlation between the vortices and the quadrupole sound sources, DMD method is used to decompose the vorticity field and Lighthill source field. The vortex is identified by the third-generation recognition technology.

The sampling duration is 0.1s from 14.9s to 15.0s, and the sampling frequency of the flow field snapshot is 1000Hz. As a result, the first three modes of the quadrupole sound source (Lighthill source) and vortices (Ω_R) are shown in Fig. 30. It can be seen that the two have a high degree of similarity in spatial distribution patterns. As a time averaged result, the 0^{th} mode shows a funnel-shaped distribution for both vortices and Lighthill source. The 1st and 2nd modes exhibit a regular wavy distribution. The higher the order, the smaller the scale of the coherent structure, and the lower the vorticity and quadrupole sound source.

Fig. 31 shows the energy proportion of the first 10 modes of vorticity and quadrupole source. It can be seen that, except for the time-averaged results of the 0^{th} mode, the first order mode accounts for more than 70 % of the total energy of the system for vorticity, and more than 85 % for quadrupole source. For the convenience of comparison, only the 1st mode is extracted for comparison in working conditions to study the correlation between vorticity and quadrupole sound sources.

Fig. 32 shows the comparison of Ω_R and Lighthill source in first-order modes at $Re = 1 \times 10^6$. It can be seen that there is a clear one-to-one correspondence between vortex pairs and Lighthill source pairs, and the two are almost identical in spatial distance. This phenomenon demonstrates the strong correlation between them.

6.3. Correlation with radiated noise

In previous studies, the leading and trailing edge noise sources were often combined into a composite load dipole (Zhang and Huang, 2023), which ignored the contribution of the wake. According to the different hydrodynamic characteristics, the trailing edge noise may be line spectrum noise or broadband noise. In this case, the boundary layer at the trailing edge is very thin, and the sound pressure here is dominated by the vortex (Ghadimi et al., 2013).

To study the correlation between vorticity and quadrupole radiation noise frequency, the mode frequencies and energies obtained by decomposing Ω_R is extracted. They are compared with the quadrupole sound pressure spectrum, as shown in Fig. 33. The hydrophone is located at 1c above the hydrofoil. It can be seen that the peak frequency of sound pressure corresponds exactly to the high-energy mode frequency of vorticity.

To investigate the correlation between vorticity and quadrupole acoustic directivity, Fig. 34 shows the quadrupole acoustic directivity of hydrofoil flow under different operating conditions. It can be seen that the high-energy direction under all four operating conditions is located downstream of the hydrofoil. Among them, there is a slight difference between a 10° angle of attack and a 15° angle of attack, with the latter having a higher energy distribution in a wider downstream range and not completely symmetrical downstream. Overall, the acoustic energy on the suction surface is greater. In addition, as the Reynolds number increases, the total sound pressure level sharply increases. This indicates that the Reynolds number has a significant impact on the quadrupole sound pressure.

The quadrupole energy is highest in the downstream direction, which is related to the wake vortex. The vortex shedding affects the quadrupole sound source, while the Lighthill source further affects the acoustic directivity of the quadrupole. To prove this point, shows the contour distribution of the Lighthill sound source on the hydrofoil at a 10° angle of attack. It can be seen that the quadrupole sound source is widely distributed downstream due to the influence of vorticity, which corresponds to the acoustic directivity.

In addition, it can be seen from Fig. 35 that as the Reynolds number increases, the density of the Lighthill sound source increases sharply, not only in the downstream length but also in the width. This also directly leads to a significant increase in the total sound pressure level of the quadrupole acoustic directivity.

7. Conclusion

The numerical research on the hydrofoil noise sources mechanism is conducted in this paper. NACA0012 hydrofoil is selected as research object. The hydrofoil drag and lift force is predicted by LES accurately. On this basis, DMD is employed to study the sound mechanisms. Some conclusions can be summarized as below:

(1) The dual-mesh technology is accurate enough to predict the underwater noise. Without considering time delay, the spectrum will experience "up drift" at high frequencies, resulting in spurious signals. The dual grid method has increased computation efficiency by more than 30 times.
(2) In terms of sound source distribution, the dipole can be divided into a 'p' term and 'dpdt' term. The larger the attack angle, the wider region of 'p' term sound source. The contribution of 'dpdt' is much smaller than the 'p' term in near fields. With attack angle, the quadrupole begins to shift towards the suction side at 5° approximately.
(3) The correlation between fluctuating pressure and dipole radiation noise is stronger at the n^{th} peak frequency. They both have maximum values in the direction of the hydrofoil suction and lifting sides.
(4) By decomposing the vortex field, it is found that the pressure fluctuation dominant mode is similar to that of the Lighthill source. The quadrupole peak frequency corresponds to the high-energy vorticity mode frequency. Besides, the quadrupole is distributed downstream widely, similar to acoustic directivity.

The research is instructive for the flow-induced-noise mechanism of submarine sail, rudder and propeller. It is beneficial to control the flow noise of hydrofoils in ships and marine engineering.

CRediT authorship contribution statement

Lianjie Yu: Writing – original draft, Visualization, Validation, Resources, Investigation, Data curation, Conceptualization. **Decheng Wan:** Writing – review & editing, Supervision, Software, Resources, Methodology, Data curation, Conceptualization. **Qi Shen:** Software. **Yan Gao:** Formal analysis. **Jiaao Geng:** Validation. **Shang Shi:** Visualization.

Data availability

The data that support the findings of this study are available from the corresponding author upon reasonable request.

Declaration of competing interest

The authors declare that they have no known competing financial interests or personal relationships that could have appeared to influence the work reported in this paper.

Acknowledgements

This work was supported by the National Natural Science Foundation of China (52131102), to which the authors are most grateful.

References

Ausoni, P., 2009. Turbulent Vortex Shedding from a Blunt Trailing Edge Hydrofoil[D]. EPFL, Lausanne, Swiss.
Bulut, S., Ergin, S., 2023. An investigation on hydro-acoustic characteristics of submerged bodies with different geometric parameters. Continuum Mech. Therm. 35 (3), 1123–1146.
Ching, Y., Jia, W., Chang, S., 2006. Design and optimization method for a two-dimensional hydrofoil. J. Hydrodyn. Ser. B 18 (3), 323–329.
Cianferra, M., Armenio, V., Ianniello, S., 2018. Hydroacoustic noise from different geometries. Int. J. Heat Fluid Flow 70, 348–362.
Daskovsky, M., 2000. The hydrofoil in surface proximity, theory and experiment. Ocean Eng. 27 (10), 1129–1159.
Del Álamo, J.C., Jiménez, J., 2009. Estimation of turbulent convection velocities and corrections to Taylor's approximation. J. Fluid Mech. 640, 5–26.
Deng, F., Wang, P., Yuan, J., Si, Q., 2025. Turbulence model comparison for ventilatedcavitation around a hydrofoil. Phys. Fluids 37, 025119.
Farassat, F., Brentner, K.S., 1998. The acoustic analogy and the prediction of the noise of rotating blades. Theor. Comput. Fluid Dynam. 10 (1), 155–170.
Gadalla, M., Cianferra, M., Tezzele, M., et al., 2021. On the comparison of LES data-driven reduced order approaches for hydroacoustic analysis. Comput. Fluids 216, 104819.
Ghadimi, P., Kermani, S., Feizi Chekab, M.A., 2013. Numerical hydroacoustic analysis of NACA foils in marine applications and comparison of their acoustic behavior. Int. Sch. Res. Not. 1, 714363.
Ghassemi, H., Ketabdari, M.J., Ashrafi, A., 2015. Numerical study on improvement of hydrofoil performance using vortex generators (research note). Int. J. Eng. 28 (2), 305–313.
He, G., Jin, G., Yang, Y., 2017. Space-time correlations and dynamic coupling in turbulent flows. Annu. Rev. Fluid Mech. 49, 51–70.
Hu, J., Wang, Z., Zhao, W., et al., 2020. Numerical simulation on vortex shedding from a hydrofoil in steady flow. J. Mar. Sci. Eng. 8 (3), 195.
Kutz, J.N., Brunton, S.L., Brunton, B.W., et al., 2016. Dynamic Mode Decomposition: Data-Driven Modeling of Complex systems[M]. Society for Industrial and Applied Mathematics.
Lockard, D., Casper, J., 2005. Permeable surface corrections for ffowcs Williams and Hawkings integrals[C]. In: 11th AIAA/CEAS Aeroacoustics Conference. Monterey, California, p. 2995.
Luo, X., Qian, Z., Wang, X., Yu, A., 2022. Mode vortex and turbulence in ventilated cavitation over hydrofoils. Int. J. Multiphas. Flow 157, 104252.
Nicoud, F., Ducros, F., 1999. Subgrid-scale stress modelling based on the square of the velocity gradient tensor. Flow Turbul. Combust. 62 (3), 183–200.
Posa, A., Broglia, R., Felli, M., et al., 2022. Hydroacoustic analysis of a marine propeller using large-eddy simulation and acoustic analogy. J. Fluid Mech. 947, A46.
Sheldahl, R.E., 1981. Aerodynamic Characteristics of Seven Airfoil Sections through 180 Degrees Angle of Attack for Use in Aerodynamic Analysis of Vertical axis Wind turbines[J]. SAND80-2114.
Smagorinsky, J., 1963. General circulation experiments with the primitive equations: I. The basic experiment. Mon. Weather Rev. 91 (3), 99–164.
Wang, Y., Mikkola, T., Hirdaris, S., 2022. A fast and storage-saving method for direct volumetric integration of FWH acoustic analogy. Ocean Eng. 261, 112087.
Wu, J., Wang, J.J., Li, T., 2013. Experimental investigation on low Reynolds number behavior of NACA0012 airfoil. J. Exp. Fluid Mech. 27 (6), 32–38.
Xu, Y., Xiong, Y., Huang, Z., 2017. Numerical study on flow induced noise of flexible hydrofoil based on fluid structure interaction. J. Huazhong Univ. Sci. Technol. (Nat. Sci. Ed.) 45 (11), 87–91+102.

Yu, A., Qian, Z., Tang, Q., Liu, J., 2022a. Numerical investigation of pulsating energy evolution in ventilatedcavitation around the NACA0015 hydrofoil. Ocean Eng. 257, 111685.

Yin, G., Ong, M.C., 2020. On the wake flow behind a sphere in a pipe flow at low Reynolds numbers. Phys. Fluids 32 (10).

Yu, L.J., Wu, J.W., Wan, D.C., 2022b. Correlation analysis between underwater noise and Liutex for DTMB4119 propeller. J. Hydrodyn. 34 (4), 585–595.

Zhang, J., Huang, Z., 2023. Transient flow and noise characteristics of accelerated flow past a hydrofoil with special emphasis on vortex-turbulence-noise interaction. Ocean Eng. 268, 113427.

Zhao, W., Pan, Z., Yu, L., et al., 2022. An overview of flow field computational methods for hydrodynamic noise prediction. J. Hydrodyn. 34 (6), 994–1005.

Zhi, Y., Huang, R., Qiu, R., Wang, Y., Huang, C., 2022. LES investigation into the cavity shedding dynamics and cavitation–vortex interaction around a surface-piercing hydrofoil. Phys. Fluids 34, 123314.